Journal of Food Processing and Preservation

WILEY

RESEARCH ARTICLE OPEN ACCESS

Bridging the Multiscale Gap: Using CFD Simulations to Translate Spray Drying Process Conditions Into a Single Droplet Drying Setup

Sebastian Höhne | Miguel Ángel Ballesteros Martínez | Torben Sträßner | Volker Gaukel

Institute of Process Engineering in Life Sciences, Food Process Engineering, Karlsruhe Institute of Technology, Karlsruhe, Germany

Correspondence: Sebastian Höhne (s.hoehne@kit.edu)

Received: 22 August 2025 | **Revised:** 14 April 2026 | **Accepted:** 5 May 2026

Academic Editor: Poulami Jha

Keywords: CFD | drying kinetics | multiscale analysis | single droplet drying | spray drying | time–temperature history

ABSTRACT

The development of industrial spray drying processes often relies on empirical studies of the impact of process and formulation parameters, as limited mechanistic insights can be gained on the morphology development of spray droplets during trials. Understanding the impact of process and formulation parameters on particle morphology is crucial for producing high-quality powder products, as the particle morphology is associated with product properties such as powder flowability. Single droplet drying methods offer the unique opportunity to directly monitor droplets during drying, expanding the mechanistic understanding of morphology development and drying kinetics of droplets. However, a major challenge of single droplet drying setups is their inability to accurately replicate time–temperature histories of droplets in spray dryers, as these histories are unfeasible to determine experimentally. To overcome this challenge, this study uses computational fluid dynamics to simulate the temperature, relative velocity, and residence time of air and particles along the spray tower. The model was validated by experimental data (primarily air outlet temperature, with air outlet velocity as a secondary check) from a pilot-scale spray dryer. Based on the simulation results, a time–temperature history was determined and applied to a hanging-droplet drying platform, allowing the independent investigation of the inlet and outlet air temperature of the spray drying process in a model environment. It was shown that the locking point can be influenced via the inlet air temperature, while final particle morphology is mainly steered by the outlet air temperature. Drying at dynamic temperature conditions is thus assumed to be crucial when investigating phenomena that are closely connected to the locking point, such as agglomeration. This study marks a crucial step toward replicating spray drying–like conditions in single droplet drying.

1 | Introduction

Spray drying is one of the most frequently used processes for food preservation and particle formation [1]. In this process, a liquid feed is converted into dry particles. To achieve this, the liquid feed is atomized into small droplets, which are rapidly dried in a hot air stream. During this drying step, particle morphology develops depending on drying conditions and feed composition. The particle morphology is known to correlate with product properties of the produced powders (e.g., smooth particles are associated with improved flowability, while more wrinkled particles potentially inhibit powder flow by interlocking) [2]. Understanding how different morphologies develop during the drying step is therefore essential for the production of high-quality powder products.

Investigating the development of the particle morphology is challenging, as the sheer number of droplets and the difficult

accessibility of industrial process equipment make a direct observation of the drying droplet virtually impossible [3]. As a result, industrial process development relies largely on empirical methods to study the impact of drying conditions on powder properties, correlating the impact of process and formulation parameters with final particle morphology while providing no mechanistic information on how the morphology developed [4]. These investigations require a substantial amount of resources, especially when executed on a larger scale, while providing little mechanistic insight. To improve process understanding, it is desired to conduct these studies in a small-scale and controlled environment. For this, a single droplet drying (SDD) experiment is commonly used. There are many different approaches for SDD, each with its own set of benefits and drawbacks [5, 6], but their underlying principle is generally the same: A single droplet is produced, which is dried in a hot air stream, and the drying progress is monitored. All approaches ultimately follow the idea that small-scale observations can be transferred to a large-scale spray drying process. To improve the applicability of these insights from model drying experiments to actual drying processes, recent research has focused on drying with dynamic temperature conditions [7, 8]. These studies involved drying of samples with changing air temperatures to mimic the dynamic temperature conditions that a droplet experiences during spray drying. A principal limitation of these approaches lies in their theoretical foundation, as the considerations concerning the temperature that a droplet experiences over the residence time are not based on experimental data. Implementing a theoretical model based on experimental data from a real spray drying process would be a crucial step in achieving more spray drying–like conditions in SDD.

This study has therefore two main objectives: First, we will determine the dynamic temperature conditions that a drying droplet experiences during its residence time in a pilot-scale spray dryer. As the time–temperature history cannot be experimentally measured, a computational fluid dynamics (CFD) simulation is used as a tool to investigate temperature conditions and residence times of the particles, based on data determined in a real spray drying process. Second, we will transfer and investigate the impact of this time–temperature history on the morphology development of droplets in an SDD process. This is an important step toward including more spray drying–like conditions in SDD. The CFD model was developed with the primary focus on the modeling of particle tracks and heat transfer. Concessions regarding the calculation of drying kinetics were made wherever reasonable to keep computing time within a sensible range. The model was validated with process parameters that could be measured experimentally, mainly the temperature and velocity of the outlet air flow. The time–temperature histories of individual particles were then obtained based on the analysis of the air and droplet temperature over the residence time and transferred to the SDD setup.

A hanging-droplet experimental setup was used for SDD, offering the advantage of a straightforward approach to investigate the morphology development, drying kinetics, and temperature during drying [9]. In these hanging-droplet setups, a liquid droplet is attached to a glass filament and dried in a hot air stream. It is expected that the time–temperature history has an impact on the morphology development and drying time in SDD. The locking point, defined as the first deviation from the initial spherical droplet shape [10], was chosen as a characteristic value to describe morphology development. It is generally assumed that the locking point is reached earlier for higher drying rates. The final particle morphology was also shown to depend on the drying rate, with higher temperatures leading to smoother particles when drying single maltodextrin (MD) droplets [8]. MD was chosen as a model system for this study as it is commonly used in the investigation of food processes, and its drying behavior is studied well. MD is a hydrocolloid, and it is therefore known to display a short constant rate period [11]. Based on this knowledge, the following hypotheses were formulated regarding the impact of dynamic drying conditions on morphology development and drying time of single MD droplets:

1. A higher initial temperature leads to a shorter time until the locking point is reached [12].
2. A higher overall temperature level leads to shorter drying times due to an overall higher drying rate.
3. A higher end temperature of the time–temperature history is expected to lead to smoother particle morphologies [8, 13].

An experimental study was conducted to investigate these hypotheses. Particles dried under the CFD-based time–temperature history are compared to particles that were dried under constant temperatures. Critical points during the morphology development of the particles were investigated, and the influence of the drying conditions on drying time was analyzed. Furthermore, the impact of drying conditions on the final morphology was investigated using scanning electron microscopy (SEM) images.

2 | Experimental Setup

2.1 | Materials

MD with a dextrose equivalent of 14 (Cargill C*DryTM MD 01910, Haubordin, France) was kindly provided by Cargill France. MD solutions with concentrations of 25, 35, and 45 wt% were prepared by adding distilled water and stirring until completely dissolved.

2.2 | Spray Tower and Experimental Trials for Model Validation

Figure 1 shows the geometry of the pilot-scale cocurrent spray dryer (Werco SD20, Hans G. Werner Industrietechnik GmbH, Germany) that was used in the CFD simulation. The spray dryer has a total height of 3 m and an inner diameter of 1.2 m. This diameter decreases to 0.1 m at the bottom of the cone, which has a height of 0.9 m. The air flow is provided to the spray tower from the top and enters the drying chamber through two concentric perforated plates. The inner distributor, centered around the nozzle, has an outer diameter of 0.24 m and an inner diameter of 0.05 m and directs around 60% of the air flow. The outer perforated plate, with an outer diameter of 1.2 m, accommodates the remaining 40 wt% of air flow. The placement of sensors for the monitoring of the inlet air temperature T_{in}, outlet air temperature T_{out}, and outlet air velocity v_{out} is also indicated in Figure 1.

Finally, the spray dryer is equipped with a cyclone separator to separate the powder from the outlet air flow.

Experiments for the validation of the CFD simulation were conducted using either distilled water or a 35 wt% MD solution at ambient temperature. The liquid feed was supplied to the spray dryer using a three-piston pump (Typ 8.5, Rannie Lab, Denmark), and atomization of the liquid feed was performed using a pressure-swirl nozzle (SKHN-MFP SprayDry, Spraying Systems Co., Germany) with an orifice diameter of 0.34 mm. An overview of the operation parameters for the validation experiments can be found in Table 1. The atomization pressure was kept constant across all trials at 50 bar. The data collection and sampling were started after the operating conditions reached a steady state, marked by the operating conditions remaining constant for at least 15 min.

The produced MD powder was collected and stored in air-tight containers for analysis. The residual moisture of the powder was determined gravimetrically with a value of 5 wt%. The measurements were performed in triplicate.

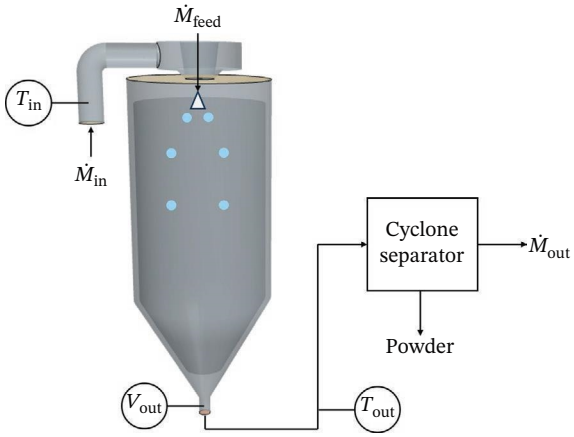

FIGURE 1 | Schematic of the pilot-scale spray dryer, indicating the placement of the sensors.

TABLE 1 | Overview of the operation parameters for spray drying trials. The heater power, air mass flow $\dot{M}_{air}$, the feed mass flow $\dot{M}_{feed}$, and the air inlet temperature T_{in} were tracked.

Feed	Heater power (kW)	$\dot{M}_{air}$ (kg/h)	$\dot{M}_{feed}$ (kg/h)	T_{in}(K)
Water	44.9	934	15	448
Water	40.4	666	15	491
MD solution	44.9	934	32	448

2.3 | SDD

2.3.1 | Hanging-Droplet Drying Platform

SDD experiments were performed in a hanging-droplet setup. For this purpose, a drying tunnel was built according to the schematic shown in Figure 2.

The drying tunnel consists of a square aluminum tube with an inner diameter of 62 × 62 mm, a wall thickness of 4 mm, and a total length of 360 mm. Pressurized air of a constant composition was used as drying gas. The volume flow rate of the drying air is controlled with a rotameter, with a maximum flow rate of $1.2 \cdot 10^{-5}$ m^3/s. Before the drying air is supplied to the drying tunnel, the air flow is directed into an air heater (RS PRO, RS Components GmbH, Germany), which is connected to a PID controller. A thermocouple at the entrance of the drying tunnel is used to control the air temperature and another one to measure the temperature in the drying tunnel. At a distance of 248 mm from the entrance of the drying tunnel, a borosilicate glass filament (Hilgenberg GmbH, Germany) with a diameter of 0.3 mm is introduced into the drying tunnel through an opening at the top. The filament is attached to a precision scale (ABP 100-5DM, Kern&Sohn GmbH, Germany) using the underfloor weighing hook. A 10-μL glass microliter syringe (Hamilton Company, Nevada, United States) is employed for the generation of 3 μL droplets. The droplets were transferred to the glass filament, immobilizing the droplet and, thus, keeping it in focus of an IDT Highspeed Os 8 digital camera (Imaging Solutions GmbH, Germany) equipped with a Sigma 150 mm f/2.8 EX DG Macro lens (Sigma Corporation, Japan) through a front window panel. Images were captured at 30 frames per second for approximately 10 min. During experimental trials, air velocity was kept constant at 0.04 m/s, and air temperature was in a range of 358–403 K. Four hundred three kelvin marks the upper limit at which a stable and precise temperature control was feasible. Air humidity was not measured during the experimental procedure. Particles with dry matter concentrations of 25, 35, and 45 wt% were dried and analyzed.

2.3.2 | Analysis of SDD Particles

The morphology development and drying time of droplets in the hanging-droplet dryer were characterized. The droplet morphology

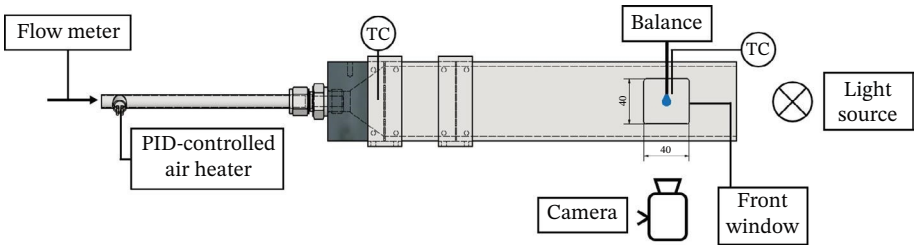

FIGURE 2 | Schematic of the hanging droplet drying setup. To observe the morphology development, the placement of a high-speed camera and light source are indicated.

was analyzed using image analysis of the recorded image data using a custom MATLAB (MATLAB R2023b, The MathWorks Inc., California, United States) script (Figure 3). Within the framework of the script, the images were binarized, and the droplet's surface area was calculated. The threshold value for the binarization was determined automatically. The binarized images were used to determine the locking point, which is defined as the moment when the droplet first deviates from its original shape.

SEM images were taken of selected particles for each parameter combination. For this, the samples were sputter-coated with 4 nm platinum at a 40° application angle. The SEM images were taken with a Leo 1530 scanning electron microscope (Gemini, Noran Instruments, Zeiss, Germany) at an acceleration voltage of 2 kV and 100× magnification. The images were made at the Laboratory for Electron Microscopy (Karlsruhe Institute of Technology, Germany). The droplet mass was recorded over the drying time to determine the drying rate. The drying time was determined as the time after which the particle reaches a solvent loading of 0.1 kg of water per 1 kg of dry matter, marking the end of the drying process.

3 | Numerical Model

The numerical model was implemented on STAR-CCM+ v.2306 (Siemens AG, Munich, Germany). As mentioned in the introduction, the objective was not to fully recreate the physical phenomena that occur inside the spray dryer but to utilize the CFD model to obtain parameters that we cannot measure in experiments: the temperature, relative velocity, and residence time of the air and drying droplets along the tower. This meant that our model configuration was guided by the philosophy of simplifying the modeling whenever possible and reasonable. For that purpose, we used the recommendations from previous numerical studies [14, 15] and focused solely on the parameters that are of actual interest for the SDD.

This philosophy led to important decisions for the numerical model. First of all, the two-phase flow inside the tower (i.e., the hot air and the liquid droplets) was simulated using a Eulerian–Lagrangian approach, which is explained in Section 3.1. Notably, the air phase is being modeled as time-steady, while the particles are being solved in a time-dependent manner, as they move through the tower. Although at first glance this might seem to present a contradiction, it is simply an alternative approach also used by previous studies [14, 16]. The reasoning is that the local transient variations caused by the effect of the particles on the air phase are rather small, and it is only their cumulative effect along the large volume of the tower that is significant. Second, we focused on the momentum and heat transfer inside the tower, so neither mass transfer nor water evaporation was considered in the modeling, but we approximated the effect of the evaporation. This is explained in Section 3.2. Section 3.3 describes how we considered the real operating conditions of the tower in the simulation, which is discussed in Section 4.1. Finally, Section 3.4 describes how we discretized the geometry of the tower and ensured that the resulting mesh did not artificially influence the results.

3.1 | Eulerian–Lagrangian Modeling of the Spray Dryer

In a spray drying process, the air is a continuum, and the droplets are discrete entities or particles. Consequently, a method is required that would allow us to solve the transport equations for a continuous phase as well as a dispersed phase. Because the volume fraction of the particles inside the tower is low, we can use a Eulerian–Lagrangian approach [14, 15, 17]. The algorithm of this method was well described by Darvan [16]. First, the transport equations for the air phase are solved over a fixed mesh (Eulerian framework) to model the behavior of the continuous phase. Then, the Lagrangian equations are used to track particles as they are carried along the flow field, based on the forces that each particle, or rather, each local cluster of particles (i.e., a parcel as explained in Section 3.1.2), experiences. Following, new volume source terms are calculated for each variable of the dispersed phase at each cell of the air flow domain, and they are added to the transport equations of the continuous phase. This procedure is repeated until the convergence criteria of coupling between the two phases are achieved [18]. An important point to mention for this solution algorithm is that we simulated the air flow as stationary to obtain direct information about the steady-state operation of the spray dryer. There was a concern that this

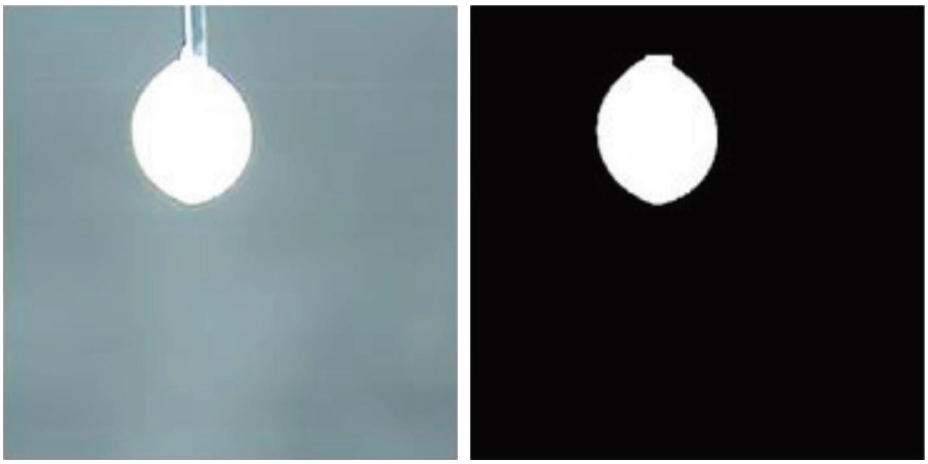

(A) (B)

FIGURE 3 | (A) Exemplary image and (B) the same image binarized using a custom MATLAB script.

simplification could affect the accurate resolution of turbulence. However, Reynolds-averaged Navier–Stokes (RANS) methods are specifically designed to resolve time-averaged flows [19]. Furthermore, the assumption of steady state has been used previously in modeling spray drying processes [14]. Even in time-dependent simulations, the approach is often to wait until pseudosteady conditions are reached before analyzing results [20, 21]. Finally, we believe that the ability to quickly solve temperature–time profiles for different particle sizes and drying conditions, which is the main objective of this paper, justifies this possible trade-off.

3.1.1 | Eulerian Modeling of the Air Phase

The air phase is assumed to be Newtonian and compressible and is modeled using the ideal-gas equation of state. In order to simulate the momentum and heat transfer in the gas phase, STAR-CCM+ solves the continuity (Equation (1)), momentum (Equation 2), and energy (Equation 3) conservation equations, which in their integral and steady-state form correspond, respectively, to [19]

$$\int_A \rho \mathbf{v} \bullet \mathrm{d}\boldsymbol{A} = \int_V S_m \,\mathrm{d}V, \tag{1}$$

$$\int_A \rho(\mathbf{v}\times\mathbf{v}) \bullet \mathrm{d}\mathbf{A} = -\int_A p\boldsymbol{I} \bullet \mathrm{d}\mathbf{A} + \int_A \boldsymbol{\tau} \bullet \mathrm{d}\mathbf{A} + \int_V \left(\mathbf{f_b} + \mathbf{S_u}\right) \mathrm{d}V, \tag{2}$$

$$\int_A \rho H \mathbf{v} \bullet \mathrm{d}\mathbf{A} = -\int_A \mathbf{q} \bullet \mathrm{d}\mathbf{A} + \int_A (\boldsymbol{\tau} \bullet \mathbf{v})\,\mathrm{d}\mathbf{A} + \int_V \left(\mathbf{f_b} \bullet \mathbf{v}\right) \mathrm{d}V + \int_V S_E \,\mathrm{d}V. \tag{3}$$

In their integral form, all terms in the equations are either integrated with respect to the volume, V in cubic meters (m^3), or the surface area, A in square meters (m^2). In the case of the latter, $\mathbf{A}$ represents the vector normal to the surface area. For Equation (1), the left side represents the convective transport. $\mathbf{v}$ is the velocity in meters per second (m/s), while ρ represents the density in kilograms per cubic meter (kg/m^3). The right side of the equation represents the volumetric source term. For this and the other equations, the source terms (S_m, S_u, and S_E) are how the influence of the Lagrangian particles is introduced into the equations. The unit of each source term corresponds to the flow rate of the transported quantity (i.e., kg/s for mass, N for momentum, or W for energy) divided by a unit volume in cubic meters (m^3). In Equation (2), the left side is also the convective transport, while the right side of the equation corresponds to the pressure gradient term, the viscous stress term, and the external body force term. Correspondingly, p is the local pressure in Pascal (Pa), $\boldsymbol{\tau}$ is the stress tensor in Pascal (Pa), $\mathbf{f_b}$ is the external force vector per unit volume in Newton per cubic meter (N/m^3), and $\boldsymbol{I}$ is the identity matrix. Finally, for Equation (3), the term on the left represents the convective transport of total enthalpy (H in J). The terms on the right account for the conductive heat flux ($\mathbf{q}$) in watts per square meter (W/m^2), the viscous work, the work from external forces, and the aforementioned source term.

This set of equations is solved using a segregated pressure-based solver, which means that the nonlinear governing equations are solved iteratively one after the other for the solution variables, such as pressure, velocity, and enthalpy or temperature. For this purpose, a pressure-implicit with splitting of operators (PISO) algorithm was implemented for the velocity–pressure coupling, and the segregated fluid enthalpy model was used to solve the total energy equation. This approach means that the equation is solved for the total enthalpy, and the temperature is then computed from enthalpy according to the equation of state [19].

Another phenomenon that had to be considered is turbulence, since the Reynolds number of the air flow inside the tower is expected to surpass 2300, based on measurements conducted at the experimental setup. Because of the assumption of steady state, an appropriate Reynolds-averaged approach for modeling the turbulence had to be selected. No additional option, such as implementing a large eddy simulation method, could be considered [22], since LES would require modeling the system as unsteady. With a Reynolds-averaging approach, the instantaneous flow velocity is decomposed into a time-averaged and a time-fluctuating component. Substituting this decomposition into Equation (2) results in the RANS equation, which has the same general form as the normal Navier–Stokes equation, apart from an additional term for the divergence of the Reynolds stresses [23], [pp. 53–71].

In principle, there are six Reynolds stress tensor components that represent the turbulence effects in all directions. These must be calculated with additional turbulence closure equations, for which a wide variety of models is available. In this work, the Reynolds stress transport (RST) was used. It is based on a set of seven equations, which allows it to simulate anisotropic and swirling flows. Given that recirculating flows are to be expected inside the tower [14], this made the RST model the most appropriate choice [15]. A more thorough explanation of what the equations that compose these models are, as well as how they are implemented into the conservation equations, is presented in Baker [23], [pp. 53–71]. To solve the pressure–strain term, the elliptic blending model by Lardeau and Manceau [24] was used, because it is compatible with the all-y^+ wall treatment that was implemented by default [19].

3.1.2 | Lagrangian Modeling of the Dispersed Droplets

As mentioned before, the trajectories of spray droplets and their essential parameters are calculated using a discrete phase model (DPM) formulated in a Lagrange framework. This means that each particle, or rather, parcel, is tracked as it "flies" through the dryer until it reaches the outlet, and its properties are recalculated at each step of its trajectory. In the case of spray dying, a parcel is a collection of droplets that are close to each other and have the same properties. Grouping the singular droplets into parcels is a necessary simplification, given the large number of droplets generated in a spray dryer, and is commonly used in these types of simulations [17]. There are two important considerations when it comes to the modeling of the droplets: how they are generated and how their trajectory is calculated.

To generate the droplets, we utilized a hollow-cone injector, located 10 cm under the top of the spray dryer (see Figure 4). The configuration of the spray cone was based on the manufacturer's information of the nozzle (see Section 2.2), as well as the atomization experiments with the same nozzle presented in Höhne et al. [25]. Most importantly, the injector was set for a

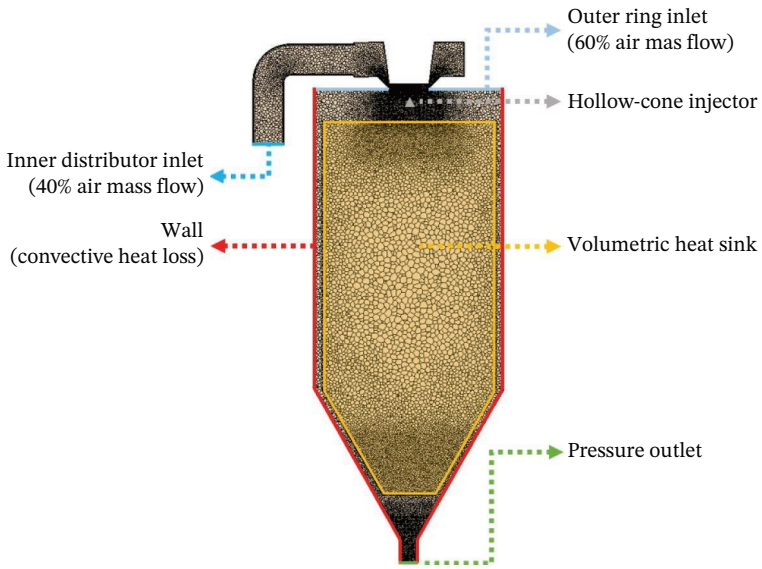

FIGURE 4 | Schematic of the boundary conditions and generated mesh.

nozzle diameter of 0.34 mm and a spray angle range of 40°–54°. The droplet sizes were assumed to follow a Rosin–Rammler distribution, with a reference size of 52 μm and a size range of 1–200 μm. Each droplet was also assigned an initial velocity based on a normal distribution, with an average of 45 m/s and a standard deviation of 1 m/s. The distribution values were selected on the assumption that the velocity of a droplet near the nozzle should be similar to that of the liquid film that generated it. The liquid film velocities were taken from Ballesteros Martínez and Gaukel [26], who simulated the internal flow of the same nozzle used in the present study. Based on the aforementioned parameters, the injector generates a set of parcels in random directions, following the spray angle restrictions and the defined size distribution. Given the direction, the velocity is obtained using the specified velocity magnitude. In steady simulations, each iteration uses the same stochastically chosen direction and size distribution. The number of parcels used is user-defined, and based on some preliminary analysis, it was set to 1000 for this study. The number of particles that are inside each parcel is adjusted by the program to ensure that the indicated mass flow is maintained.

Once the particles are created, it is important to correctly calculate the trajectory and movement of the particles, especially given the turbulent behavior of the air flow. The particles are assumed to be spherical and of a fixed size. Therefore, the change in their momentum can be calculated every timestep as the sum of the forces acting on them. Five different forces are taken into account in this calculation [17]. The first one is the gravitational force associated with the particle's mass. The second one is the drag force of the air on the droplets, which is calculated using the Schiller–Naumann correlation [27]. The third one is the shear lift caused by the velocity gradient of the exiting air, which is calculated according to the Sommerfeld method [28]. The fourth one is the force of the surrounding pressure gradient on the particle volume. The final one is the force that is exerted on the particle as it accelerates the surrounding air phase, which is calculated using a virtual mass model [29]. It should be noted that, while the formation and movement of the particles were simulated, neither collision nor secondary-breakup models were included.

In addition to the trajectory of the particles and their balance of forces, the heat transfer between the particles and the air was important for this study. However, given that we did not account for evaporation in the modeling, some workarounds had to be included in the model. This is explained in Section 3.2.

3.1.3 | Two-Way Coupling of the Continuous Air and Dispersed Droplets

As there is a two-way coupling between the Eulerian and Lagrangian formulations, the effect of the particles on the continuous phases must also be considered. For this purpose, the particles are included as momentum, mass, and energy volumetric sources in the transport equations. This approach assumes that the cell volume is large compared to the particle size [19], which may not always be the case for the thin cells near the walls or in refined regions. Therefore, to ensure a stable solution, a volumetric source smoothing method was introduced, namely, the cell cluster method. With it, STAR-CCM+ spreads the effect of each Lagrangian particle over a cluster of cells when the particle size approaches that of the surrounding cells.

An important topic that might have been noticed by the reader is that the air phase is being modeled as time-steady, while the particles are being solved in a time-dependent manner, as they move through the tower. How the approach works is by iterating between solving the flow field of the air phase and (re)calculating the trajectories and properties of the parcels along the entire tower. Between iterations, the updated trajectories are used to calculate new heat, force, and mass source terms that are then included in the set of equations of each of the cells through which the particles have moved. As a simplified example, one can imagine the trajectory of a given particle crosses through a mesh cell, where the air phase has a higher temperature than the particle. The trajectory is calculated from the initial pressure

and velocity field of the air flow. Based on the relative velocity between the phases, the particle size, and the residence time inside the cell, the algorithm calculates the amount of heat that is transferred to the particle from the air in that specific cell. This heat is then included as a source (or rather, sink) term in the energy equation of the same cell, for the next iteration. With this information, new temperature, velocity, and pressure fields are calculated for the air flow. In turn, these new fields lead to a corrected particle trajectory, and the heat-transfer calculations are then repeated. The iterations are carried out until the conservation equations of both the Eulerian and Lagrangian formulations converge [16].

3.2 | Modeling Heat Transfer Between the Particles and the Air

As mentioned before, the mass transfer and, therefore, the evaporation were not included in the simulation. The reasoning for this is that drying kinetics, even of simple model systems such as MD solutions, are a complex and still active area of research [30]. Moreover, the most commonly used drying models, such as the reaction engineering approach (REA) or the characteristic drying curve (CDC), are all semiempirical [31]. In the case of REA, which is the model implemented in STAR-CCM+, the water evaporation is modeled as a chemical reaction, with an activation energy that increases as moisture content decreases [32]. However, the parameters of the correlation between activation energy and moisture content still have to be established experimentally and can vary depending on the feed composition and the drying conditions [19]. In the case of CDC, it accounts for the two different drying stages by including a retardation factor that decreases the mass transfer coefficient once the locking point is reached. Nonetheless, the locking point must also be first determined experimentally and depends on feed composition and drying conditions [30]. All these model parameters are, in fact, usually established using SDD setups [33–35].

Given that the objective of the simulations was to gain insight from the process inside the spray tower to replicate them in the SDD setup, it seemed counterproductive to use information obtained from an SDD setup as a basis for the simulation. With that in mind, we utilized a simplified approach in which the latent heat of evaporation is accounted for in the specific heat capacity of the injected particles. That means that the heat capacity of the particles greatly increases as they reach the wet-bulb temperature, and it decreases again as they heat up above it. This allows us to take the drying step of the particles into account for the modeling of the heat transport. The calculated values for the "apparent" heat capacities are shown in Table 2. For the simulations with only water, the standard heat capacities of water and steam were used. For the simulation with an MD solution, the specific heat capacity was calculated using the water content of the liquid feed and the sprayed powder, assuming the specific heat capacity of pure water to be 4.2 kJ/kg·K and that of pure MD to be 2.4 kJ/kg·K. To include the specific enthalpy of evaporation of 2257 kJ/kg in the apparent heat capacity, the value of the evaporation enthalpy was divided by the range of the wet-bulb temperature of 2 K over which the drying step occurs. Furthermore, the changing dry matter content and residual moisture are considered. Under the conditions inside the spray dryer, the wet-bulb temperature was determined based on the inlet air conditions and a Mollier diagram for air [36]. An interesting consequence of this approach is that it is assumed that the drying of the particles happens only under a constant-rate period. This might cause the drying times to be shorter than the ones in the real spray dryer but should still provide valuable information with regard to the trajectories, temperatures, and residence times that the droplets experience.

TABLE 2 | Specific heat capacities (C_p) used in the simulation to calculate both the sensible heat as well as the evaporation enthalpy at the wet-bulb temperature. The evaporation enthalpy is integrated in the apparent specific heat capacities for temperatures of 316–318 K.

	Specific heat capacity (kJ/kg·K)		
Material	**< 316 K**	**316–318 K**	**> 318 K**
Water	4.2	1226.7	1.8
MD solution	3.6	736.0	2.3

3.3 | Boundary and Operating Conditions of the Spray Dryer

The boundary conditions set for the simulation are shown in Figure 4. As explained in Section 2.2, around 40% of the air mass flow is fed to the tower through an inner annular distributor that surrounds the nozzle. The rest is delivered uniformly through an outer perforated plate. These real inlet conditions had to be represented in the simulation. The injector was located at the same height as the nozzle, which is located in the pilot tower, at around 10 cm from the top. At the bottom of the spray tower, a pressure outlet was located. The walls of the spray dryer were assumed to allow heat loss to the environment. The ambient temperature was set as 294 K. When particles collide with the wall, a rebound condition is in place for the particles.

After initial validations of the simulation, we found that the wall condition alone cannot remove the amount of heat that is lost to the environment according to the experimental measurements. The results are discussed in detail in Section 4.1, but, in short, performing an energy balance with the experimental data obtained when spray drying water, we concluded that significantly more heat is dissipated into the environment than what the convective heat transfer alone could achieve in the simulation. This is most likely due to additional heat transfer phenomena, like conduction through the metal supports and foundation, as well as radiation. In order to correct for this, without artificially raising the heat flux at the wall, we included a heat sink that uniformly subtracted the additional heat loss all across the internal volume. The amount of heat that is getting subtracted via this heat sink is based on a heat balance across the whole spray drying process and takes all heat losses into account. The described additional heat transfer phenomena are summarized by a correction term that translates to the heat sink. This heat sink was calibrated with the experimental results to achieve a realistic outlet air temperature. To ensure that this approach would not cause unrealistic conditions, we validated the simulation by comparing the resulting air velocity at the outlet with experimental data. This is also discussed in Section 4.1.

3.4 | Mesh Generation

The internal volume of the spray dryer and the air distributor were meshed using a polyhedral mesh. Since polyhedral cells are multifaceted, they are connected to a high number of neighboring cells, which allows a robust approximation of transport gradients [37]. The resulting mesh is shown in Figure 4. Given the large scale of the spray dryer, the mesh was refined in regions of interest (i.e., in the region near the nozzle, the internal air distributor, and the conical outlet at the bottom). It should be noted that thin prismatic cells were generated near the wall all around the geometry to better approximate the boundary layer [38].

A mesh independence test was carried out to define the optimal cell size. This test is based on running several simulations of the same system under the same conditions with decreasing cell sizes, until a predefined convergence criterion reaches a stable value [39], pp. 1–8. With that in mind, we generated four meshes using the parameters shown in Table 3.

They all differed in reference cell size, while the number of prism layers was kept constant. The cell sizes were chosen to be equally spaced between 1.25 and 2 mm. The thickness of the first layer was calculated to make sure that its y^+ (i.e., the dimensionless wall distance relative to the viscous wall layer as defined by Schlichting and Gersten [40], [pp. 519–610]) was below one.

The convergence criteria were the outlet air temperature and velocity of the spray tower operating at maximum velocity and inlet temperature but without any liquid injection or heat sink. The resulting values can be seen in Figure 5. It can be noticed that at cell sizes below 1.75 cm, the cell sizes have only a little effect on the properties of the outlet air. Considering this, a cell size of 1.5 cm was deemed sufficient to ensure mesh independence for all the simulations in this study. With such a mesh fineness, the numerical error caused by the spatial discretization seems to be reduced reasonably. Therefore, further refining the mesh beyond this value would bring no benefits and would only negatively affect the simulation efficiency.

TABLE 3 | Mesh parameters. ROIs refer to regions of interest: nozzle, air distributor, and conical outlet.

Parameter	Value
Reference cell size/cm	1.25–2.0
Refining factor for ROIs	0.33
No. of prism layers	8
Thickness (y^+) of the first layer	10 μm (0.04)
Max. growth rate	1.5

4 | Results and Discussion

This study focuses first on the results of the CFD-based determination of the time–temperature history of a droplet in a pilot-scale spray dryer and then on the application and impact of these dynamic drying conditions on morphology development and drying time in an SDD process. The simulation results are supported by experimental data gaind in spray drying trials. Basic correlations of boundary conditions on process conditions have been shown a number of times in literature and are therefore not specifically shown here. The temperature and velocity profiles inside the spray tower are calculated and presented in Section 4.1. In Section 4.2, the particle tracks are evaluated, and key values of the time–temperature histories are determined in Section 4.3. These results are then used in Section 4.4 to transfer a spray drying–like time–temperature history on the SDD setup and investigate its influence on the locking point, drying time, and final morphology.

4.1 | Simulation of the Temperature and Velocity Profiles Inside the Spray Tower

To validate the CFD model, the simulation was run with water and MD feeds and compared to experimental results. The heat loss was adjusted based on the simulations with water and then applied to the simulation using the MD solution as feed. An overview of the parameters that were used for the validation of the simulation is given in Table 4. Simulations were run at the same inlet air temperatures, T_{in}, and air mass flows, $\dot{M}_{air}$, as in the experimental trials. The outlet air temperature, T_{out}, was used as the main validation parameter, while the outlet air velocity, v_{out}, was utilized to check the plausibility of the simulation. For this, average values over the cross-sectional area are taken. In general, the simulation values (Sim) show good agreement with the experimental values (Exp) for all parameters and feed combinations. At first glance, the simulated outlet temperature for water with $T_{in} = 491$K might seem slightly higher than the experimental measurement. However, the experimental result still falls within the variation

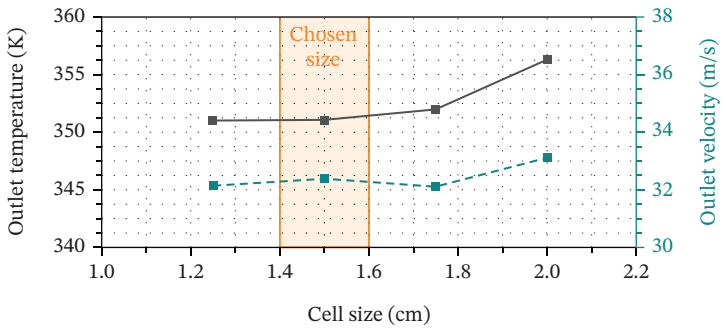

FIGURE 5 | Effect of the cell size on the outlet air temperature (left axis and gray straight line) and velocity (right axis and green dashed line).

TABLE 4 | Overview of the experimental and simulation results of the parameters utilized for simulation validation. It should be noted that the standard deviation of the simulation results is a spatial deviation over the 843 cells of the spray dryer outlet cross-section.

			T_{out}(K)		v_{out}(m/s)	
Feed	T_{in}(K)	$\dot{M}_{air}$(kg/s)	**Exp**	**Sim**	**Exp**	**Sim**
Water	448	0.26	361	363 ± 4	33	33.5 ± 4
Water	491	0.19	351	358 ± 9	23	23 ± 3
MD solution	448	0.26	353	351 ± 4	34	32 ± 3

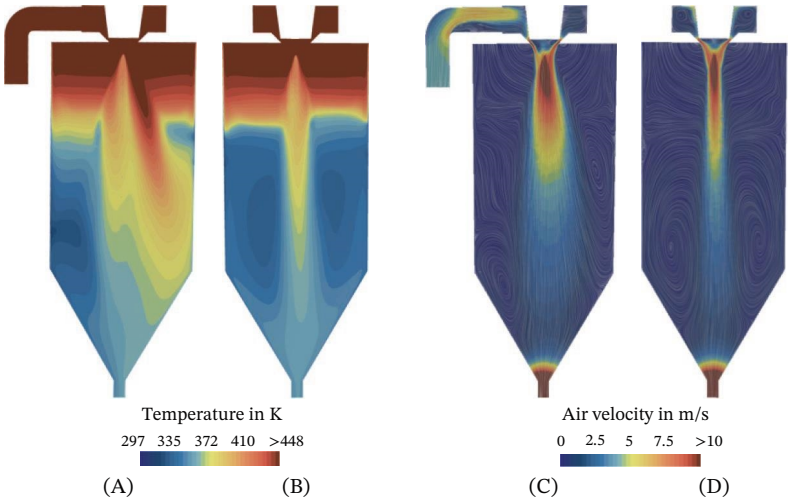

FIGURE 6 | (A, B) Calculated temperature and (C, D) velocity profiles of the air in the spray tower. Views from (A, C) the front and (B, D) the right side. The simulation was carried out at $T_{in} = 448$ K and $M_{air} \doteq 0.26$ kg/s.

range of the simulated values (±9 K). Furthermore, the deviation can be attributed to the experimental measurement being taken at a single point, as well as possible insulation of the thermocouple by MD powder. It is important to note that model calibration only against T_{out} is not ideal. However, installing additional sensors into the spray tower was not feasible, as the presence of not completely dry spray droplets in the upper section of the spray tower leads to significant fouling problems on any sensors. Nonetheless, this limitation was deemed acceptable, as the primary goal of this study is to provide a proof of concept on how dynamic time–temperature history can affect SDD experiments.

Figure 6 shows the CFD-derived temperature (Figure 6A,B) and velocity (Figure 6C,D) profiles within the pilot plant spray dryer. The profiles are shown from the front (Figure 6A,C) and the right-hand side (Figure 6B,D). The simulation with MD particles was carried out at $T_{in} = 448$ K and $\dot{M}_{air} = 0.26$ kg/s. Both of the front views (Figure 6A,C) show that the profiles are asymmetrical. This is especially apparent for the temperature profile (Figure 6A). The profile exhibits a gradient from the top, with a temperature of 448 K, to the bottom of the spray tower, where a temperature of around 351 K is reached. The temperature profile also shows a jet of hot air in the center of the drying chamber, which feathers out toward the right side, while the left side shows lower temperatures. The front view of the velocity profile (Figure 6C) gives a hint toward the source of this asymmetry. A total of 60 wt% of the drying air enters the air distributor from the left side and is then directed through the inner annular plate. This leads to the formation of the jet with velocities of up to around 10 m/s, which conserves some of the momentum through the air distributor into the drying chamber and toward the right-side wall. This leads to the observed slight asymmetry of the velocity of the center jet but also creates different flow patterns on either side of the center jet. The higher volume flow of air toward the right side of the spray dryer likely leads to higher temperatures in this part. What might add to this effect is the observation of a large vortex on the right side of the center jet. When comparing the position of vortices in the drying chamber (Figure 6C) to the temperature profile (Figure 6A), it can be observed that these regions exhibit higher temperatures than the regions above the vortices. This is in contrast to the vertical temperature gradient at the center of the spray dryer. Figure 6B,D shows the views from the right-hand side of the spray dryer. Both profiles are more symmetrical than Figure 6A,C, further supporting the assumption that the asymmetry is introduced by the inlet direction of the air flow into the air distributor. The asymmetry of the air flow is also indirectly observed in experimental trials, where higher amounts of powder are deposited on the right side of the drying chamber compared to the left side. Considering these observations, a droplet's time–temperature history appears to heavily depend on its specific track within the spray dryer. This is especially important when particles are distributed more within the spray tower. Furthermore, the observed asymmetry has significant implications when scaling up to industrial dryer designs. For these dryers with a different length-to-diameter ratio, the simulation results could reveal potential zones of air recirculation, powder deposition, or dead zones.

4.2 | Investigation of Particle Tracks

The paths of particles were simulated and tracked through the spray dryer, with the results shown in Figure 7 for $T_{in} = 448\,K$, $\dot{M}_{air} = 0.26\,kg/s$, and the feed being MD solution. To evaluate the time–temperature history of the drying particles, the heat transfer to the particles and, thus, the virtual drying progress were tracked. The color of the particle tracks is used to visualize the drying progress of the particles; red indicates that the particle is in the drying step, while blue signals the initial heating step and the period after completion of drying. To improve readability, the transition between the stages is marked in yellow. The results for all particles of the simulation are depicted in Figure 7A, while tracks for three random particles with particle sizes of approximately 20, 60, and 100 μm each are presented in Figure 7B–D. The particle tracks originate from the position of the nozzle orifice and are simulated with different initial spray angles and directions. Starting from the top, the spray pattern is initially relatively symmetrical. After around 20% down the vertical axis of the drying chamber, an asymmetry of the spray forms. The spray appears to be pushed toward the right side of the drying chamber. This observation fits well with the results of the velocity profile in Figure 6, which indicates that the center air jet is directed toward the right side of the dryer.

Looking into the results for different particle sizes (Figure 7B–D), it can be observed that the spray is narrower for smaller particles and wider for larger particles. Furthermore, the simulation of larger particles also appears to display a longer and, therefore, wider initial spray cone, indicating that a larger mass and, therefore, inertia of the particles also lead to a wider distribution of particles in the spray dryer. Nonetheless, as only a few selected particles are depicted here, the impact of spray angle cannot be completely excluded. To decouple the impact of the spray angle from the particle size, monodisperse simulations with a larger number of particles were conducted for 60 and 100 μm (Figure A1). The results show the same general spray pattern compared to Figure 7C,D but also reveal different collision patterns and the number of particles colliding with the spray dryer wall depending on particle size. Particles colliding with the dryer wall can also be observed on the right-side wall in Figure 7A. In the monodisperse simulations (Figure A1), particles with a size of 60 μm collide with the wall on the right side of the dryer, while 100 μm particles show wall contact on both sides of the dryer, with more particles on the right side. This pattern of powder deposition was also observed in the experimental validation trials. The total number of collisions, n_{col}, was $n_{col} = 23$ for $x = 60\,\mu$m and $n_{col} = 89$ for $x = 100\,\mu$m. These results also provide quantitative information about the collision and indirect deposition of particles on the dryer wall by correlating the particle–wall collisions with the drying progress. This becomes evident when considering 100 μm particles, as it can be observed that these particles can hit the wall while still drying, posing an increased risk of sticking to the dryer wall. Overall, the results shown in Figure 7 revealed the particle size as one of the main drivers for particle distribution in the spray dryer.

Figure 7B–D shows the impact of the particle size on the tracks of particles through the spray dryer for particle sizes of 20–60 μm. Overall, a strong dependency of the particle tracks on the particle size can be discerned. Smaller particles with $x \approx 20\,\mu$m follow tracks closely along the vertical axis of the spray dryer, while the particles distribute more in the spray dryer with increasing particle size. To investigate this observation in more detail, relative velocities between the air and particles are plotted over the residence time, as shown in Figure 8. It can be seen that the relative velocities decrease from over 25 m/s to less than 0.5 m/s for all particle sizes. The particles have a high initial velocity of about 45 m/s, which is rapidly decreasing in the much slower air flow, with velocities of up to around 10 m/s. The sharpest decrease is observed for small particles with $x \approx 20\,\mu$m, reaching $v_{rel} < 0.5\,m/s$ in under 0.01 s, whereas the same velocity is reached for large particles with $x \approx 100\,\mu$m after around 0.1 s. This is likely due to the differences in mass and, therefore, inertia of the particles, leading to a longer time to adjust to air velocity for large particles compared to small particles. The longer equalization time of particle and air velocity also translates to a more pronounced impact of spray angle and entry direction on the particle tracks. No clear trend for the impact of the particle size on the residence time can be discerned based on the particle tracks (Figure 7) and results for the relative velocity (Figure 8). While the particle tracks indicate a wider spread and longer travel distances for larger particles, the relative velocities show that larger particles take longer to slow down to the velocity of the air.

The residence time, depending on the particle size, is analyzed with the results plotted in Figure 9. A general trend toward longer residence times with increased particle size is observed, indicating that the impact of the size distribution of the particles on the residence time is more significant than the slower adjustment of particle velocity. Additionally, the residence times appear to vary more

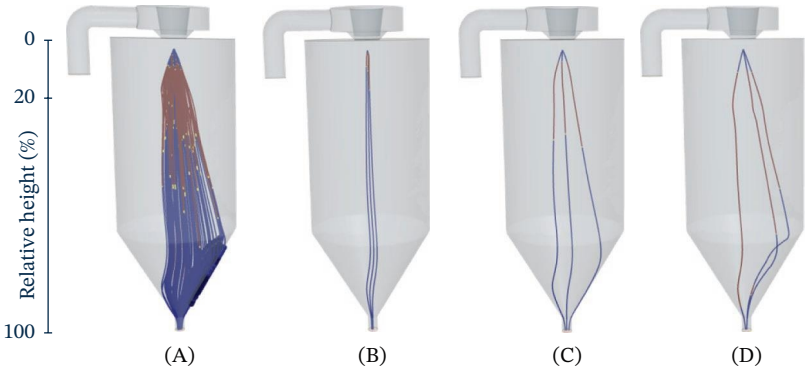

FIGURE 7 | Particle tracks of (A) all particles and (B) 20, (C) 60, and (D) 100 μm for $T_{in} = 448\,K$ and $\dot{M}_{air} = 0.26\,kg/s$.

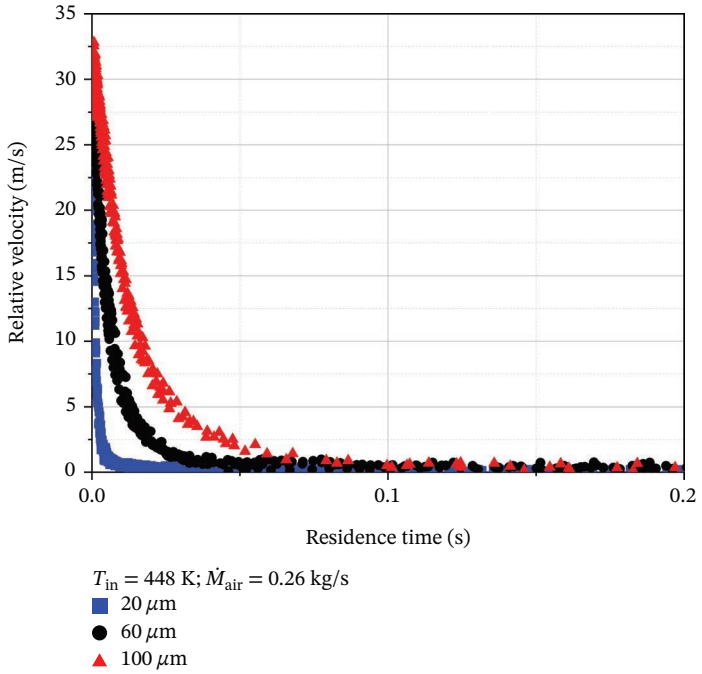

FIGURE 8 | Relative velocity of the particles and surrounding air for different particle sizes for a simulation with $T_{in} = 448\,K$ and $\dot{M}_{air} = 0.26\,kg/s$.

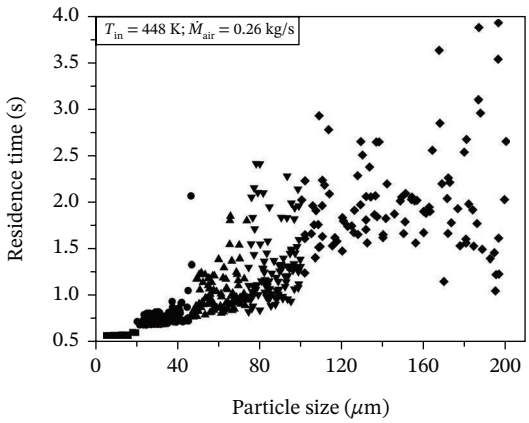

FIGURE 9 | Residence time over the particle size for a simulation with $T_{in} = 448\,K$ and $\dot{M}_{air} = 0.26\,kg/s$.

with increasing particle size. This is likely due to a greater variation in the particle tracks. Small particles follow a relatively consistent track along the vertical axis of the spray tower (Figure 7B), while larger particles show greater dependency on spray angle and entry direction (Figure 7C,D). This effect is only further exacerbated by the increasing number of particles that collide with the dryer wall, leading to a reduction of particle velocity and, thus, an increased residence time.

4.3 | CFD-Based Time–Temperature History and Transfer to SDD

It was shown in Section 4.2 that particle tracks depend on particle size, spray angle, and entry direction. Furthermore, the inhomogeneous, asymmetric temperature and velocity profiles (Section 4.1) were found, further reinforcing the notion that particles can experience quite different temperature conditions. It is therefore necessary to define characteristic temperature values correlated with the drying progress that are representative for the majority of particles. To achieve this, the first step is the determination of the effect of particle size on drying time (Section 4.3.1), to set a reference value for the average drying time. Section 4.3.2 then evaluates the air and particle temperature over the drying time to determine key air temperature values over the drying process. These results are then extrapolated to SDD times and transferred to the experimental setup in Section 4.3.3 by fitting the air temperature to the CFD-based time–temperature history.

4.3.1 | Effect of the Particle Size on Drying Time

The drying time is investigated to determine an endpoint for the time–temperature history. Two different inlet air temperatures and air mass flows were investigated to examine the robustness of the calculated parameters. It is expected that drying time increases with increasing particle size, as well as lower inlet air temperature and air mass flow. The results for the average drying time over the particle size are presented in Figure 10. The results show an increasing drying time with increasing particle size for all investigated drying conditions. When looking at the impact of the air inlet temperature and the air mass flow, the drying time increases with a decrease in either parameter. The trends that the drying time shows for different boundary conditions are physically sound and according to expectation. For the determination of the time–temperature history, the drying time t_{end} at the standard drying conditions of $T_{in} = 448\,K$ and $\dot{M}_{in}$ for particles of 100 μm was taken as a reference, which was calculated to be $t_{end} = 0.86\,s$ on average. Due to the particles drying solely during the constant rate period in the CFD model, t_{end} represents a minimum value of the drying time, as mass transfer slows down during the falling rate period and leads to longer drying times in an experimental study.

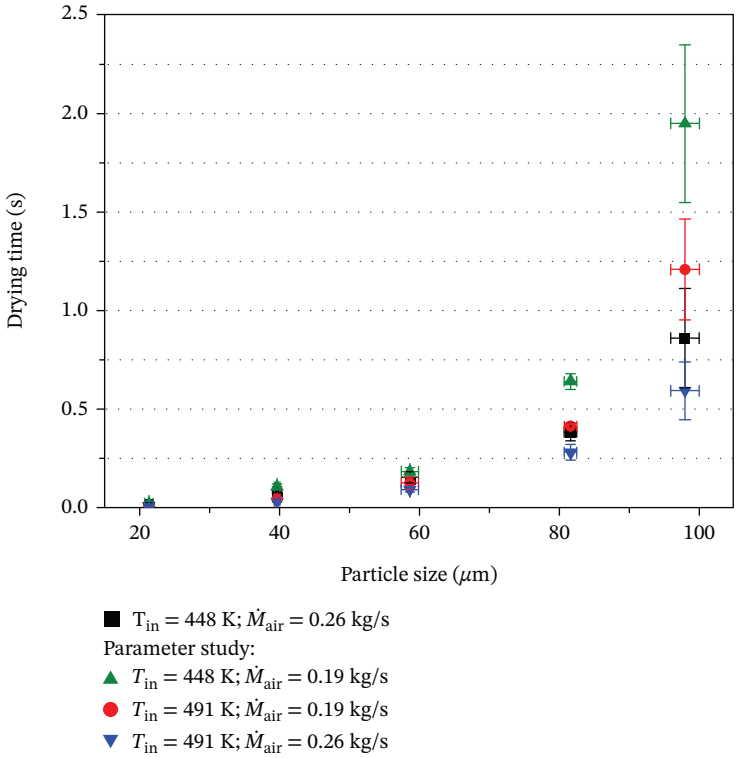

FIGURE 10 | Drying time over the particle size for all simulation conditions using a polydisperse spray.

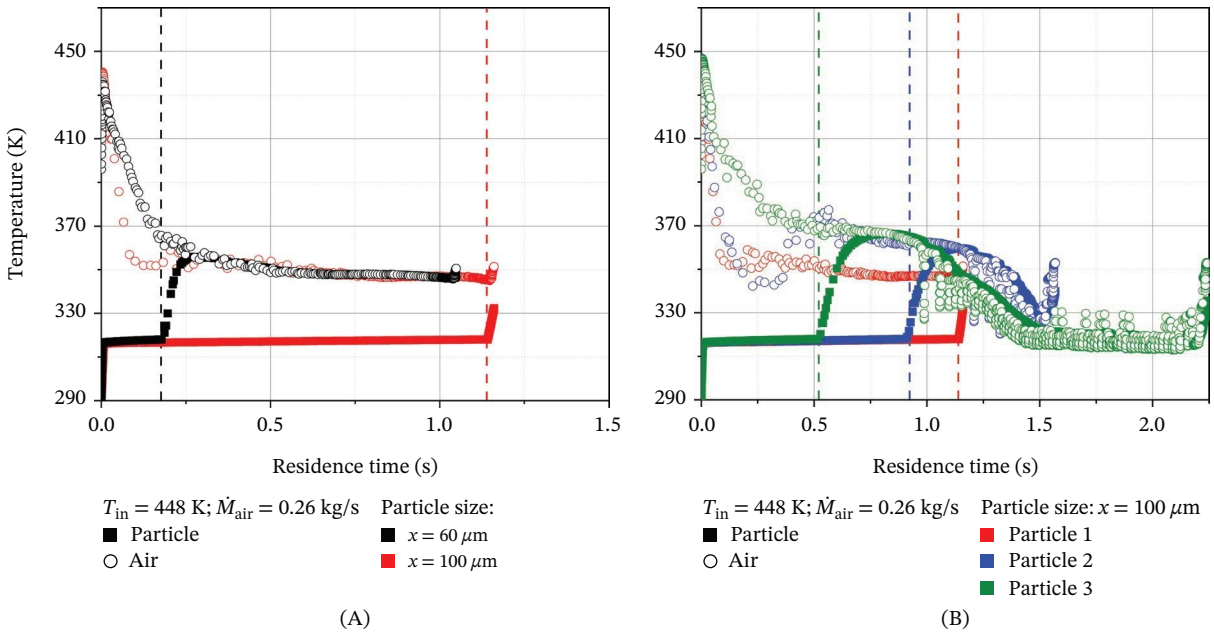

FIGURE 11 | Particle and air temperature over the residence time for particles of (A) $x = 60\mu$m and $x = 100\mu$m and three particles of (B) $x = 100\mu$m. The time after which drying concludes is marked by dashed, vertical lines. Simulation run for a maltodextrin feed with $T_{in} = 448$ K and $\dot{M}_{air} = 0.26$ kg/s.

4.3.2 | Investigation of Air and Particle Temperature Over the Residence Time

Figure 11 shows the results for the temperature of specific particles and air around the particle over the residence time in the spray tower. Results for different particle sizes (60 and 100 μm) are presented in Figure 11A, while the results for multiple particles of $x = 100\,\mu$m are presented in Figure 11B. The drying endpoint for each particle is marked by a vertical dashed line in the diagrams. Results for particle sizes of 20 μm are omitted from this due to two reasons: First, the drying times are very short, making a visual comparison of the data challenging, and second, droplets in SDD are much larger than in spray drying, making large particles in the CFD simulation

more interesting for analysis of the time–temperature histories. Focusing on the result of the particle temperature T_p with a particle size of $x = 60\,\mu$m first, it can be observed that the initial temperature shows a sharp increase until the wet-bulb temperature is reached. At this point, the specific heat capacity of the particle increases, and the virtual drying step begins. T_p remains almost constant until the drying step is concluded, after which T_p rises until T_{air} is reached. The development of T_p over the residence time is in principle the same for $x = 100\,\mu$m, with two main differences. First, the drying and residence times are longer for $x = 100\,\mu$m. Second, which is a difference specific to the analyzed particle with $x = 100\,\mu$m, T_p does not reach T_{air}, as the particle leaves the spray dryer shortly after drying is concluded. The drying air temperature T_{air} is generally relatively similar for both particle sizes but decreases faster for $x = 100\,\mu$m. This is expected to be a result of the difference in particle size, with larger particles having a higher surface area and, thus, faster initial heat exchange.

To translate the time–temperature history of spray drying to SDD, the largest particles are typically prioritized, in this case, $x = 100\,\mu$m. These particles are critical when pushing the spray drying boundaries, that is, when drying at high dry matter concentrations, as incomplete drying can lead to wall deposition and, thus, reduced run times in industrial processes. Furthermore, their size is closest to the particle size in SDD, making their drying behavior most comparable. Hence, the time–temperature history will be derived from particles of around $x = 100\,\mu$m.

The temperature of the air and multiple particles with $x = 100\,\mu$m are depicted in Figure 11B, with the corresponding tracks shown in Figure 7D. As was anticipated, due to the asymmetric temperature and velocity profiles in the spray dryer, every particle has a unique residence time, drying time, and consequently time–temperature history. For example, Particle 2 shows a dip in temperature after a residence time of around 0.25 s. It is assumed that the particle moves through a cold spot of the drying chamber, demonstrating the high dependency on local temperature conditions. Such cold spots can also be observed in the heterogenous temperature profile shown in Figure 6A,B, making it likely that the particle passed through a cold spot before entering a zone of higher temperature again. Furthermore, the temperature of Particle 3 shows a lower temperature than T_{out} after drying and before exiting the spray dryer, which is likely caused by contact with the dryer wall. Due to the uniqueness of the individual particles, it is necessary to find key temperature values that represent the general time–temperature history of as many particles as possible. For this, only particles that conclude drying before wall collision or exiting the spray dryer are considered. To begin with, the particles generally experience an initial temperature of around $T_{in} = 448$ K. The temperature rapidly declines, reaching a plateau after around 0.15 s, which is after around 17.5% of the drying progress when taking the average drying time of 0.86 s into account (see Section 4.3.1). Typically, the air temperature remains relatively constant around 358 K until drying concludes. These key temperature values, depending on the relative drying progress, are used as a reference for the temperature control in the SDD setup in Section 4.3.3.

4.3.3 | Comparison of Different Air Temperature Control Concepts

To transfer the time–temperature history to the SDD setup, different air temperature control concepts were compared experimentally. The target drying end time, to which the CFD-based time–temperature history was extrapolated, was $t_{end} = 275$ s for 35 wt% MD droplets dried at constant $T_{SDD} = 358$ K. Based on the CFD results, the starting temperature should decrease to the outlet temperature after 17.5% of the total drying time, which equates to 48 s based on the experimental t_{end}. Figure 12 shows these critical points of the time–temperature history as a function of temperature over time. The time–temperature history is used as a reference for the two investigated air temperature control concepts. The drying channel is preheated to the highest possible temperature of 403 K for both control concepts. In Control Concept 1, the PID controller of the air heater is simply set to $T = 358$ K right after the droplet is attached to the glass filament. Meanwhile, Control Concept 2 is based on the work of Eijkelboom et al. [8], where a second cold air stream is used. To emulate this, the initial hot air stream is switched to a cold air supply with $T = 298$ K. The results of both control concepts show a similar decrease in temperature until a drying time of around 10 s. Afterwards, the temperature of Control Concept 2 exceeds the lower limit of 358 K rapidly, making a precise control of the drying temperature very challenging. Control Concept 1 does not overshoot the temperature of 358 K, reaching a temperature of 361 K after 50 s, giving a satisfactory match of the CFD-based time–temperature history critical points. This is exacerbated by the fact that the drying times calculated by the CFD model should be shorter, as the particles are assumed to completely dry during the constant rate period. Therefore, Control Concept 1 was chosen over Control Concept 2 for the further experimental SDD study.

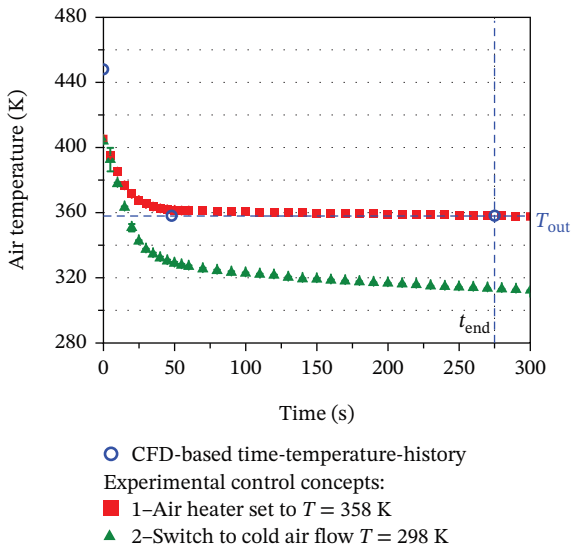

FIGURE 12 | Fit of the experimental air temperature over time to the characteristic data of the air temperature derived from the simulation. Experimental air temperature was measured at the position of the droplet in the SDD setup.

4.4 | Impact of a CFD-Based Time–Temperature History on SDD

4.4.1 | Impact of the Time–Temperature History on the Time to the Locking Point

The results for the investigation of the impact of the time–temperature history on the locking point of drying droplets are depicted in Figure 13. Based on the understanding that the locking point is reached relatively early during drying of MD droplets, it is assumed that the drying rate in the early stages of the process is critical. This leads to the expectation that the locking point is reached earlier for higher temperatures, as solutes concentrate at the droplet's surface more rapidly. Continuing this line of thought, if the locking point is reached while the final temperature of the dynamic time–temperature history is not yet reached, it is expected that the time to the locking point should be relatively similar between droplets dried at constant 403 K and droplets dried dynamically at 403 K and a final temperature of 358 K. Furthermore, the locking point at a constant temperature of 358 K is expected to be reached later compared to both a constant temperature of 403 K or a dynamic temperature. This study was conducted for MD concentrations of 25, 35, and 45 wt% to ensure a robust impact of the different time–temperature histories on the drying of the particles.

Taking a look at the results for a constant temperature of 358 K first, it can be seen that the time to the locking point decreases with increasing MD concentration from around 35 s for 25 wt% to around 5 s at 45 wt%. This is according to the expectation. Compared to the results for a constant drying temperature of 403 K, the time to the locking point is much shorter, with a value of around 16.5 s for 25 wt% MD droplets. Taking a look at the dynamic time–temperature history at the same concentration, the time to the locking point is about 15.4 s. This value is almost identical to the result of using a constant temperature of 403 K, showing that the time to the locking point mainly depends on the initial temperature experienced by a droplet. The results demonstrate that a dynamic time–temperature history can have a significant impact on the locking point of a droplet. The locking point is known to be a crucial parameter steering agglomeration, and including dynamic temperature conditions could be crucial for a mechanistic investigation of the agglomeration step, which is already an active field of research [41]. Extending these findings on the spray drying process points toward a greater impact of the inlet air temperature on the time to the locking point compared to the air outlet temperature. This insight could be used for industrial process optimization. The locking point is directly related to the stickiness of the powder, which is a crucial parameter when deficits regarding agglomeration or yield loss of the product are observed. A precise control of the locking point could help minimize powder wall deposition, maximizing product yield and dryer run times in industrial settings.

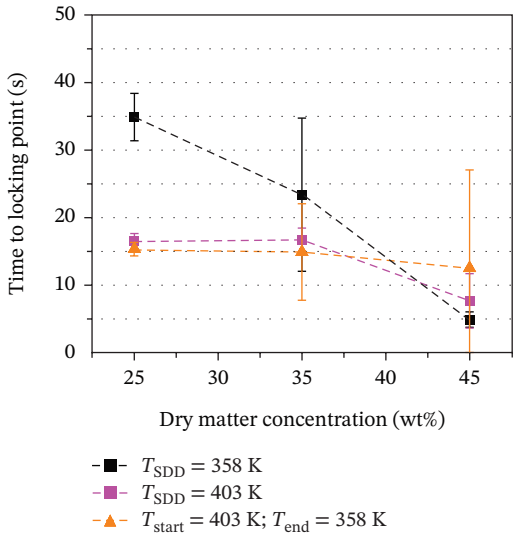

FIGURE 13 | Time to the locking point over dry matter concentration for different time–temperature histories.

4.4.2 | Impact of the Time–Temperature History on Final Drying Time

Figure 14 shows the comparison of dynamic and constant temperature conditions on the drying time across different initial MD concentrations. It is expected that drying time decreases when drying at conditions that lead to overall higher temperatures [42]. Looking at the impact of the different temperature conditions, it can be seen that the drying time decreases with an increase in air temperature from 358 to 403 K for all MD concentrations, as expected. When the drying temperature is changed from 403 to 358 K during the process, the drying time is between the drying times for the two constant drying temperatures. This is attributed to a larger initial drying rate of the particles compared to a constant temperature of 358 K but a lower overall drying rate compared to a constant 403 K. Contrary to the assumption that higher dry matter concentrations lead to shorter drying times, the results indicate that the MD concentration has little impact on the drying time of the particles. Even though the constant rate period is likely shorter with increasing MD concentration, the drying time consequently appears to be dominantly governed by the falling rate period. This leads to, on

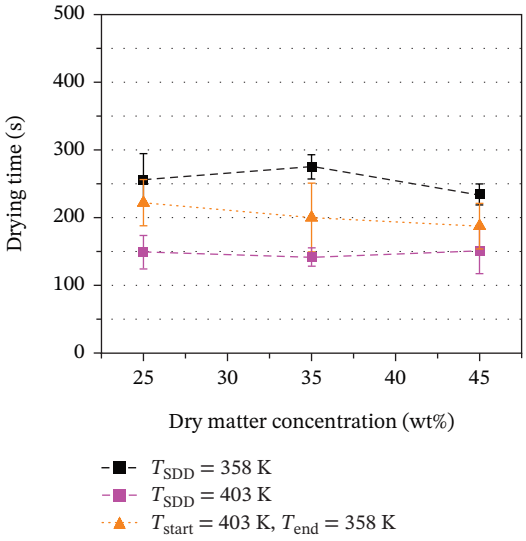

FIGURE 14 | Comparison of the drying time until a water load of $X = 0.1 kg_{H2O}/kg_{DM}$ is reached over the dry matter concentration for different time–temperature histories.

average, lower drying rates and overall similar drying times for the different dry matter concentrations.

4.4.3 | Impact of the Time–Temperature History on Final Particle Morphology

SEM micrographs of particles from SDD are shown in Figure 15. The impact of a dynamic time–temperature history compared to particles dried at a constant temperature was investigated for different MD concentrations. Looking first at results for 25 wt% MD concentration (Figures 15A, 15D, and 15G), the particle dried at $T = 358$ K exhibits a wrinkled surface, consistent with observations by Both et al. [43] who reported smooth particles at 298 K and increasingly wrinkled particles with increasing temperature up to 363 K. But, conversely in our experiment with increasing temperatures ($T = 403$ K), particles exhibit a smooth, cracked surface. This observation is likely due to particles dried at 358 K continuously shrinking, while particles dried at 403 K are observed to inflate during the drying process (see Figure A2). This particle inflation is also in line with the results from Eijkelboom et al. [8], who showed that particles dried at 493 K inflate more than particles dried at 353 K while also appearing smoother. For the dynamic time–temperature history, a wrinkled morphology is observed, similar to the morphology dried at 358 K, indicating that the end temperature is crucial for morphology development during drying. Furthermore, comparing the particles dried with a dynamic time–temperature history with particles dried at a constant 403 K shows that the use of a dynamic history can have a significant impact on final particle morphology. This highlights that careful consideration of the drying conditions is crucial when investigating the morphology development in SDD as a model for spray drying. Translating these results to the spray drying process would mean that changing the outlet temperature during drying has a greater impact on final morphology than changes in the inlet temperature. It has to be noted, however, that the CFD model does not explicitly model physical phenomena such as mass transfer, glass transition, or viscosity effects. A more sophisticated model that includes these phenomena could result in a slightly different time–temperature history, which could affect SDD results.

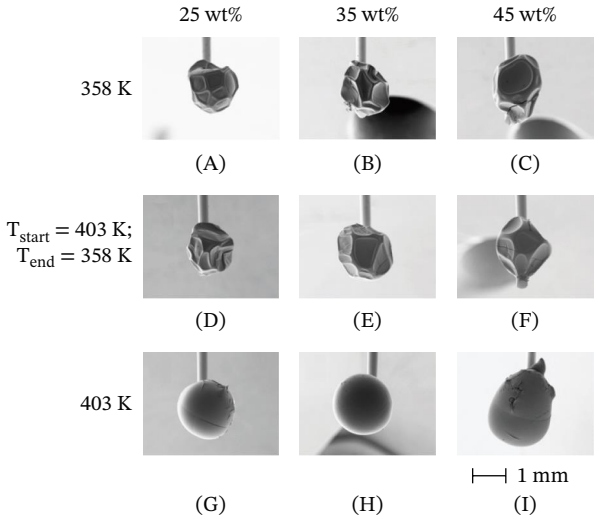

FIGURE 15 | (A–I) SEM pictures of maltodextrin particles dried in SDD with different time–temperature histories and dry matter concentrations.

Taking different matrix material concentrations into account, only slight differences can be observed. Particle size increased, and sphericity decreased with increasing MD concentration. However, the morphology of the particle, meaning the smoothness of the particle surface, does not show an obvious correlation with MD concentration. Although both higher matrix material concentrations and higher initial temperatures lead to an earlier locking point (Figure 13), a shorter drying time is only observed for higher temperatures (Figure 14). At higher drying rates, the final particle morphology is established rapidly, leading to larger, smoother particles. At lower drying rates, the particle skin stays in a viscous state for a longer duration, allowing more wrinkling. Changing the matrix material concentration, however, has no major impact on the time that the drying particles stay in a viscous state, and, thus, no clear impact on the final morphology. Ultimately, the insights gained on the control of the final particle morphology could be used to reveal potential links to the flowability of industrial powders.

5 | Conclusions

In this study, a representative time–temperature history was determined for drying droplets in a spray dryer, and the conditions were transferred to an SDD setup. Subsequently, the impact of this dynamic temperature control on morphology development and drying time was investigated, comparing it to constant temperatures that are typically used in SDD. To achieve this, a simplified CFD model of a pilot-scale spray dryer was designed and validated. The model was used to determine the temperature and velocity profiles of the air flow in the spray tower, as well as the tracks and drying progress of the particles. The model showed that larger particles showed a wider spray pattern within the spray tower and take a longer time until they slow down to the air velocity compared to smaller particles. Furthermore, the model provided physically sound correlations of drying conditions and drying time, as drying time decreases with higher initial air temperature and air mass flow for all particle sizes. The model also revealed that each particle shows a unique track and, thus, time–temperature history in the spray dryer. Identifying suitable, universally applicable characteristic values to describe this history was therefore critical. Our findings show that the temperature of the drying air sharply decreased for around 17.5% of drying time, after which the droplet experiences a relatively constant temperature. This time–temperature history was extrapolated to SDD times and replicated by fitting the experimental temperature control to the identified characteristic values.

SDD with a dynamic time–temperature history showed an impact on the locking point for droplets with low MD concentration. At this concentration, the locking point was reached earlier when drying with a high initial temperature and a lower end temperature. Notably, the time to the locking point was almost identical compared to droplets dried solely at the higher temperature. This result shows a critical impact of the starting temperature on the locking point. Transferring this observation to

the spray drying process, the inlet air temperature is expected to correlate with the locking point of spray droplets. Drying at a dynamic time–temperature history showed no clear impact on the locking point at higher MD concentrations. These findings demonstrate the relevance of including a dynamic time–temperature history when investigating phenomena linked to the early stages of droplet drying, such as agglomeration, wall deposition, or yield loss.

With respect to the impact of the time–temperature history on drying time, it was found that a higher initial temperature leads to shorter drying times consistent across all investigated dry matter concentrations, showing a clear impact of the time–temperature history on drying rates. Finally, the particle morphology was mainly determined by the end temperature (T_{end}) of the drying process, exhibiting a wrinkled surface for lower temperatures and a smooth surface for higher temperatures. In the context of spray drying, it is expected that the outlet air temperature would correlate with final particle morphology.

In summary, the determined time–temperature history successfully enabled the investigation of the impact of both the inlet and outlet air temperature in a spray dryer. This study marks a crucial first step toward achieving spray drying–like conditions in SDD, validated by pilot-scale spray drying data. Going forward, the time–temperature history could be refined by increasing the complexity of the CFD model, integrating a more sophisticated drying model, which would be able to model key physical phenomena such as mass transfer, glass transition, and droplet shrinkage, similar to studies found in literature [20, 44, 45]. More importantly, this study opens new pathways to investigate the impact of drying conditions on powder properties and advances the mechanistic understanding of the spray drying process.

Nomenclature

Latin Symbols

A	surface area, m^2
A	vector normal to the surface area, –
c_p	specific heat capacity, J/(kg·K)
f	external force vector per unit volume, N/m^3
H	total enthalpy, J
H	identity matrix, –
$\dot{M}$	mass flow, kg/s
p	pressure, Pa
q	heat flux, W/m^2
S	source term, –
T	temperature, K
t	total drying time, s
V	volume, M^3
v	velocity, m/s

Acknowledgments

The authors express their gratitude to Markus Fischer, Pablo Oviedo Cogorno, and Jonas Kaltenbach for the experimental support.

Funding

This study was funded by the Bundesministerium für Wirtschaft und Energie, 10.13039/501100006360, 21662 N, and the International Fine Particle Research Institute, 10.13039/100017562. Open Access funding enabled and organized by Projekt DEAL.

Conflicts of Interest

The authors declare no conflicts of interest.

Data Availability Statement

The data that support the findings of this study are available from the corresponding author upon reasonable request.

References

1. A. M. Goula, T. Varzakas, and C. Tzia, "Dehydration Spray Drying—Freeze Drying," in *Handbook of Food Processing: Food Preservation* (Taylor & Francis, 2016), 158–221, https://doi.org/10.1201/b19397-6.

2. D. E. Walton, and C. J. Mumford, "Spray Dried Products—Characterization of Particle Morphology," *Chemical Engineering Research and Design* 77, no. 1 (1999): 21–38, https://doi.org/10.1205/026387699525846.

3. C. Sadek, P. Schuck, Y. Fallourd, N. Pradeau, C. le Floch-Fouéré, and R. Jeantet, "Drying of a Single Droplet to Investigate Process–Structure–Function Relationships: A Review," *Dairy Science & Technology* 95, no. 6 (2015): 771–794, https://doi.org/10.1007/s13594-014-0186-1.

4. M. A. I. Schutyser, J. Perdana, and R. M. Boom, "Single Droplet Drying for Optimal Spray Drying of Enzymes and Probiotics," *Trends in Food Science & Technology* 27, no. 2 (2012): 73–82, https://doi.org/10.1016/j.tifs.2012.05.006.

5. N. M. Eijkelboom, A. P. van Boven, I. Siemons, et al., "Particle Structure Development During Spray Drying From a Single Droplet to Pilot-Scale Perspective," *Journal of Food Engineering* 337 (2023): , https://doi.org/10.1016/j.jfoodeng.2022.111222111222.

6. N. Fu, M. W. Woo, and X. D. Chen, "Single Droplet Drying Technique to Study Drying Kinetics Measurement and Particle Functionality: A Review," *Drying Technology* 30, no. 15 (2012): 1771–1785, https://doi.org/10.1080/07373937.2012.708002.

7. M. Schugmann, and P. Foerst, "Concept, Design, and Measurement Methodology of a Highly Dynamic Thin Film Dryer for Experimental *In Situ* Drying Manipulation," *Review of Scientific Instruments* 93, no. 6 (2022): , https://doi.org/10.1063/5.0083295065108.

8. N. M. Eijkelboom, K. Gawronska, J. M. Vollenbroek, et al., "Single Droplet Drying With Stepwise Changing Temperature-Time Trajectories: Influence on Heat Sensitive Constituents," *Food Research International* 182 (2024): , https://doi.org/10.1016/j.foodres.2024.114194114194.

9. M. A. I. Schutyser, E. M. Both, I. Siemons, E. M. J. Vaessen, and L. Zhang, "Gaining Insight on Spray Drying Behavior of Foods via Single Droplet Drying Analyses," *Drying Technology* 37, no. 5 (2019): 525–534, https://doi.org/10.1080/07373937.2018.1482908.

10. I. Siemons, R. G. A. Politiek, R. M. Boom, R. G. M. van der Sman, and M. A. I. Schutyser, "Dextrose Equivalence of Maltodextrins Determines Particle Morphology Development During Single Sessile Droplet Drying," *Food Research International* 131 (2020): , https://doi.org/10.1016/j.foodres.2020.108988108988.

11. I. Zbiciński, and X. Li, "Conditions for Accurate CFD Modeling of Spray-Drying Process," *Drying Technology* 24, no. 9 (2006): 1109–1114, https://doi.org/10.1080/07373930600778221.

12. B. R. Bhandari, E. D. Dumoulin, H. M. J. Richard, I. Noleau, and A. M. Lebert, "Flavor Encapsulation by Spray Drying: Application to Citral and Linalyl Acetate," *Journal of Food Science* 57, no. 1 (1992): 217–221, https://doi.org/10.1111/j.1365-2621.1992.tb05459.x.

13. S. Shamaei, A. Kharaghani, S. S. Seiiedlou, M. Aghbashlo, F. Sondej, and E. Tsotsas, "Drying Behavior and Locking Point of Single Droplets Containing Functional Oil," *Advanced Powder Technology* 27, no. 4 (2016): 1750–1760, https://doi.org/10.1016/j.apt.2016.06.006.

14. M. Mezhericher, A. Levy, and I. Borde, "Three-Dimensional Spray-Drying Model Based on Comprehensive Formulation of Drying Kinetics," *Drying Technology* 30, no. 11-12 (2012): 1256–1273, https://doi.org/10.1080/07373937.2012.686136.

15. L. Huang, K. Kumar, and A. S. Mujumdar, "Simulation of a Spray Dryer Fitted With a Rotary Disk Atomizer Using a Three-Dimensional Computional Fluid Dynamic Model," *Drying Technology* 22, no. 6 (2004): 1489–1515, https://doi.org/10.1081/drt-120038737.

16. A. Darvan, *CFD Simulation of Spray Drying Process Using a New Droplet Drying Kinetics* (PhD Diss., Martin-Luther-Universität, 2016).

17. S. Blei, and M. Sommerfeld, "CFD in Drying Technology–Spray-Dryer Simulation," in *Modern Drying Technology*, 1st ed. (Wiley, 2011), 155–208, https://doi.org/10.1002/9783527631629.ch5.

18. G. Kohnen, M. Rüger, and M. Sommerfeld, "Convergence Behaviour For Numerical Calculations By The Euler/Lagrange Method For Strongly Coupled Phases," *Numerical Methods in Multiphase Flows* 185 (1994): 191–202.

19. Siemens Industries Digital Software, "Simcenter STAR-CCM+ User Guide, Version 2036," (2023), https://www.siemens.com/en-us/company/about/businesses/digital-industries/.

20. J. V. Bürger, M. Jaskulski, and A. Kharaghan, *CFD Studies of Agglomeration and Coalescence in Spray Drying With Fines Return* (Jiangnan University, 2024).

21. J. Xiao, S. Yang, O. A. George, A. Putranto, W. D. Wu, and X. D. Chen, "Numerical Simulation of Mono-Disperse Droplet Spray Dryer: Coupling Distinctively Different Sized Chambers," *Chemical Engineering Science* 200 (2019): 12–26, https://doi.org/10.1016/j.ces.2019.01.030.

22. B. Blocken, "LES Over RANS in Building Simulation for Outdoor and Indoor Applications: A Foregone Conclusion?," *Building Simulation* 11, no. 5 (2018): 821–870, https://doi.org/10.1007/s12273-018-0459-3.

23. C. Baker, T. Johnson, D. Flynn, et al., *Train Aerodynamics* (Butterworth-Heinemann, 2019), https://doi.org/10.1016/B978-0-12-813310-1.00007-1.

24. S. Lardeau, and R. Manceau, *Computations of Complex Flow Configurations Using a Modified Elliptic-Blending Reynolds-Stress Model* (10th International ERCOFTAC Symposium on Engineering Turbulence Modelling and Measurements, 2014).

25. S. Höhne, M. L. Taboada, J. Schröder, C. Gomez, H. P. Karbstein, and V. Gaukel, "Influence of Nozzle Geometry and Scale-Up on Oil Droplet Breakup in the Atomization Step during Spray Drying of Emulsions," *Fluids* 9, no. 3 (2024): 70, https://doi.org/10.3390/fluids9030070.

26. M. A. Ballesteros Martínez, and V. Gaukel, "Using Computation Fluid Dynamics to Determine Oil Droplet Breakup Parameters during Emulsion Atomization with Pressure Swirl Nozzles," *Fluids* 8, no. 10 (2023): 277, https://doi.org/10.3390/fluids8100277.

27. L. Schiller, *Über die grundlegenden Berechnungen bei der Schwerkraftaufbereitung* (Zeitschrift des Vereines deutscher Ingenieure, 1933).

28. M. Sommerfeld, "Theoretical and Experimental Modelling of Particulate Flows," *Technical Report Lecture Series 2000-06 von Karman Institute for Fluid Dynamics* (von Karman Institute for Fluid Dynamics, 2000).

29. T. R. Auton, J. C. R. Hunt, and M. Prud'Homme, "The Force Exerted on a Body in Inviscid Unsteady Non-Uniform Rotational Flow," *Journal of Fluid Mechanics* 197 (1988): 241–257, https://doi.org/10.1017/S0022112088003246.

30. J. V. Bürger, M. Jaskulski, and A. Kharaghani, "Modeling of Maltodextrin Drying Kinetics for Use in Simulations of Spray Drying," *Drying Technology* 43, no. 1-2 (2025): 214–227, https://doi.org/10.1080/07373937.2024.2421451.

31. E. Boel, R. Koekoekx, S. Dedroog, et al., "Unraveling Particle Formation: From Single Droplet Drying to Spray Drying and Electrospraying," *Pharmaceutics* 12, no. 7 (2020): 625, https://doi.org/10.3390/pharmaceutics12070625.

32. X. D. Chen, and G. Z. Xie, "Fingerprints of the Drying Behaviour of Particulate or Thin Layer Food Materials Established Using a Reaction Engineering Model," *Food and Bioproducts Processing* 75, no. 4 (1997): 213–222, https://doi.org/10.1205/096030897531612.

33. S. X. Qi Lin, and X. D. Chen, "Improving the Glass-Filament Method for Accurate Measurement of Drying Kinetics of Liquid Droplets," *Chemical Engineering Research and Design* 80, no. 4 (2002): 401–410, https://doi.org/10.1205/026387602317446443.

34. T. T. H. Tran, M. Jaskulski, J. G. Avila-Acevedo, and E. Tsotsas, "Model Parameters for Single-Droplet Drying of Skim Milk and Its Constituents at Moderate and Elevated Temperatures," *Drying Technology* 35, no. 4 (2017): 444–464, https://doi.org/10.1080/07373937.2016.1182548.

35. R. Huelsmann, W. Wiggers, G. J. Esper, and R. Kohlus, "Single Droplet Investigation on the Levitator to Explain the Drying Kinetics and Morphology Formation of Maltodextrin DE <3 and DE 21," *Drying Technology* 41, no. 6 (2023): 989–1009, https://doi.org/10.1080/07373937.2022.2125988.

36. M. Virkkunen, M. Kari, V. Hankalin, and J. Nummelin, *Solid Biomass Fuel Terminal Concepts and a Cost Analysis of a Satellite Terminal* (Julkaisija–Utgivare, 2015), https://doi.org/10.13140/RG.2.1.3865.3921.

37. M. Sosnowski, J. Krzywański, and R. Gnatowska, *Polyhedral Meshing as an Innovative Approach to Computational Domain Discretization of a Cyclone in a Fluidized Bed CLC Unit* (E3S Web of Conferences, 2017), https://doi.org/10.1051/e3sconf/20171401027.

38. K. Okumura, "CFD Simulation by Automatically Generated Tetrahedral and Prismatic Cells for Engine Intake Duct and Coolant Flow in Three Days," in *SAE Technical Paper Series* (SAE International, 2000).

39. H. K. Versteeg, and W. Malalasekera, *An Introduction to Computational Fluid Dynamics: The Finite Volume Method*, 2nd ed. (Pearson/Prentice Hall, 2007).

40. H. Schlichting, and K. Gersten, *Boundary-Layer Theory* (Springer, 2017), https://doi.org/10.1007/978-3-662-52919-5.

41. A. P. Van Boven, N. M. Eijkelboom, K. J. Fentsahm, et al., "A Multiscale Investigation on Protein Addition Toward Steering Agglomeration and Yield in Spray Drying," *LWT - Food Science and Technology* 212 (2024): , https://doi.org/10.1016/j.lwt.2024.116998116998.

42. T. T. H. Tran, J. G. Avila-Acevedo, and E. Tsotsas, "Enhanced Methods for Experimental Investigation of Single Droplet Drying Kinetics and Application to Lactose/Water," *Drying Technology* 34, no. 10 (2016): 1185–1195, https://doi.org/10.1080/07373937.2015.1100202.

43. E. M. Both, A. M. Karlina, R. M. Boom, and M. A. I. Schutyser, "Morphology Development During Sessile Single Droplet Drying of Mixed Maltodextrin and Whey Protein Solutions," *Food Hydrocolloids* 75 (2018): 202–210, https://doi.org/10.1016/j.foodhyd.2017.08.022.

44. T. T. H. Tran, M. Jaskulski, and E. Tsotsas, "Reduction of a Model for Single Droplet Drying and Application to CFD of Skim Milk Spray Drying," *Drying Technology* 35, no. 13 (2017): 1571–1583, https://doi.org/10.1080/07373937.2016.1263204.

45. M. Buchholz, J. Haus, S. Pietsch-Braune, F. Kleine Jäger, and S. Heinrich, "CFD-Aided Population Balance Modeling of a Spray Drying Process," *Advanced Powder Technology* 33, no. 7 (2022): , https://doi.org/10.1016/j.apt.2022.103636103636.

Appendix A

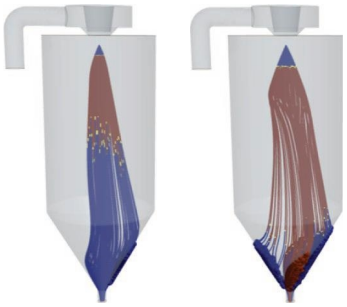

FIGURE A1 | Particle tracks for a simulation with a monodisperse spray of (A) 60 μm and (B) 100 μm for a simulation with $T_{in} = 448$ K and $\dot{M}_{air} = 0.26$ kg/s.

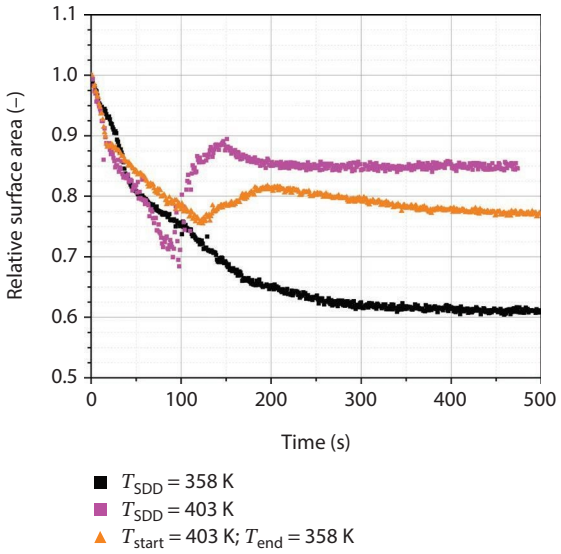

FIGURE A2 | Relative particle size at the end of drying over the dry matter concentration for different time-temperature histories.